

Phenylenediamine-Derived Carbon Dots for Carbon-Based Supercapacitors

Melis Ozge Alas Colak,* Ahmet Güngör,* Suleyman Gokhan Colak, Rukan Genc,* and Emre Erdem

In the present investigation, multicolor fluorescent carbon dots (CDs) are produced using *meta* (m-PD), *ortho* (o-PD), and *para* (p-PD) phenylenediamine isomers as precursors. These CDs display bright and stable green, yellow, and red fluorescence under ultraviolet light excitation, with variations in photoluminescence emissions attributed to differences in particle size and bandgap. The CDs from o-PD, m-PD, and p-PD are thoroughly characterized using techniques such as UV-vis spectroscopy, fluorescence emission spectroscopy, transmission electron microscopy, a zeta sizer, Fourier Transform Infrared Spectroscopy, and Raman spectroscopy. As electrode materials in a two-electrode system for

symmetric supercapacitors, the performance of CDs is examined, revealing that m-PD-derived CDs (m-CDs) exhibit superior electrochemical properties. Specifically, m-CDs achieve a specific capacitance of 72.3 F g^{-1} at 0.1 A g^{-1} , an energy density of 1.00 Wh kg^{-1} , and a power density of 9.41 kW kg^{-1} . The enhanced performance of m-CDs is attributed to an increase in electropositivity and faster electron mobility associated with smaller particle sizes. This research highlights the potential of utilizing PD-derived CDs to enhance the electrochemical performance of supercapacitors, demonstrating significant advancements in energy storage technology.

1. Introduction

The selection of electrode materials highly influences the performance of supercapacitors (SCs), as they play a crucial role in determining key parameters, such as energy density, power density, and cycling stability.^[1–4] Among various electrode candidates, carbon-based materials have attracted significant interest due to their high specific surface area, excellent electrical conductivity, and structural robustness. These properties enable efficient charge storage and fast ion transport, which are essential for high-performance SCs. Electrode materials, such as metal oxides,^[5] sulfides,^[6] carbon-based materials,^[7] and conductive polymers,^[8] are actively used in SCs. Unlike some transition metal

oxides and conducting polymers, which can suffer from limited power density or long-term stability, carbon nanomaterials, including carbon nanotubes, fullerenes, and carbon dots (CDs), offer a promising alternative.^[1,9–11] CDs, in particular, stand out due to their tunable surface chemistry, environmental friendliness, and potential for low-cost, scalable synthesis. Integrating CDs into SCs is, therefore, a crucial strategy for developing sustainable and efficient carbon-based electrode materials and advancing next-generation energy storage technologies.

CDs, a type of zero-dimensional carbon nanoparticle, have garnered attention due to their low toxicity, cost-effectiveness, biocompatibility, and excellent photoluminescence.^[12–14] Composed of nanosized sp^2 hybridized graphitic cores and carbonyl

M. O. Alas Colak, R. Genc
SUNUM Nanotechnology Research Centre
Sabanci University
TR-34956 Istanbul, Turkey
E-mail: melisalas@mersin.edu.tr
rgenc@mersin.edu.tr


M. O. Alas Colak, R. Genc
Department of Chemical Engineering
Engineering Faculty
Mersin University
TR-33343 Mersin, Turkey


A. Güngör, E. Erdem
Faculty of Engineering and Natural Sciences
Sabanci University
TR-34956 Istanbul, Turkey
E-mail: ahmet.gungor@sabanciuniv.edu

A. Güngör, E. Erdem
Center of Excellence for Functional Surfaces and Interfaces for
Nano-Diagnostics (EFSUN)
Sabanci University
Orhanlı, Tuzla, 34956 Istanbul, Turkey

S. G. Colak
Department of Biomedical Engineering
Faculty of Engineering and Natural Sciences
Iskenderun Technical University
31200 Hatay, Turkey

R. Genc
Research and Application Center
Mersin University Advanced Technology Education
33343 Mersin, Turkey

 Supporting information for this article is available on the WWW under <https://doi.org/10.1002/batt.202500364>

 © 2025 The Author(s). Batteries & Supercaps published by Wiley-VCH GmbH. This is an open access article under the terms of the Creative Commons Attribution License, which permits use, distribution and reproduction in any medium, provided the original work is properly cited.

surface moieties, CDs are used in biochemical sensing, fluorescence probes, photocatalysis, and drug delivery.^[12,14,15] Their adjustable surface chemistry, efficient electron transfer, and wide light-harvesting range make them suitable for energy storage and conversion applications, including ion batteries, solar cells, and optoelectronics.^[16,17] CDs enhance ion and electron transport in SCs by increasing the contact area between the electrode and electrolyte, thus improving electrochemical performance.^[18] Therefore, in many studies, CDs have been used in pure or composite forms as carbon-based electrode materials in SCs to improve electrochemical performance. In previous studies by our group, the potential of CDs and composite structures based on them as electrode materials in SCs has been investigated. In a study carried out, multicolored CDs were synthesized from cola drinks, and α -MnO₂/PPy hybrid nanorods modified with these CDs were evaluated as anode materials in hybrid SCs. The electrodes used in the designed sandwich-type SC provided a maximum area capacitance value of 17.3 $\mu\text{F cm}^{-2}$.^[19] In addition, we utilized manganese (II)-doped CD-PANI composites as electrode materials in the designed Swagelok-type SC, achieving a specific capacitance of 595 F g^{-1} .^[14] In another study, we synthesized surface oxygen-enriched CDs with hyperbranched bis-MPA polyester hydroxyl polymers (HBPs). We demonstrated that the number of hydroxyl groups plays a crucial role in enhancing the capacitance performance of CDs. The surface oxygen-enriched CDs exhibited a higher specific capacitance value of 32.08 F g^{-1} compared to pure CDs (19 F g^{-1}).^[16]

It has been reported that synthetic precursors affect the physical and chemical properties of CDs.^[20] Precursors rich in aromatic amines and phenols, such as phenylenediamine (PD) isomers or o-dihydroxybenzene, are frequently used in the production of CDs with high quantum yield (QY), multicolor, and long-wavelength emission.^[21–23] PD, which has three types of isomers: ortho-PD, meta-PD, and para-PD, is a crucial precursor for producing many heterocyclic compounds and polymers. Regarding aromatic diamines, PD derivatives containing more nitrogen atoms are notable for their versatility in functionalizing a free amino group. Additionally, the high conjugation of these isomers leads to increased luminescence, particularly fluorescence. Researchers used PD derivatives, which have an aromatic ring and nitrogen as a heteroatom, as precursors and reported that CDs prepared from PD exhibited long-wavelength fluorescence.^[24,25] Moreover, it has been reported that PD derivatives are suitable molecules for the functionalization of organic materials, such as carbon nanotubes, graphene oxide, metal organic framework (MOF), and carbon spheres, and are effective in improving the performance of SCs.^[26–30] In our recent works, we investigated the impact of PD isomers in the nanomaterial development process and their potential for use as electrode materials in SCs. In one of our studies, it was observed that copper zinc tin sulfide (CZTS)/x-PD nanocomposites, produced by integrating PD (x: o-PD, m-PD, and p-PD) isomers into the kesterite structure of CZTS, exhibited significant improvements in electrochemical performance as PD-based electrodes. CZTS/p-PD nanocomposites exhibited superior performance with a specific capacitance value of 424.6 F g^{-1} at a current density of 0.1 A g^{-1} and showed excellent

cyclic stability by maintaining 95.5% of this capacitance after 10,000 cycles.^[31] Finally, we used PD as an organic comonomer material to enhance the low cycle number and cyclic stability of conductive polymer polyaniline (PANI) and improve its electrochemical properties. When PANI P(ANI-co-oPD) copolymerized with oPD was used as an electrode, the resistance decreased, and a significant specific capacitance of 541.7 F g^{-1} was achieved with considerable energy and power density values of 7.5 Wh kg^{-1} and 23.9 kW kg^{-1} , respectively.^[32]

In our previous study, a specific capacitance value of 32.08 F g^{-1} was obtained when CDs were used directly as SC electrode materials without forming composites, revealing the necessity of improving performance. In this direction, considering the effect of PD, which is known to play a crucial role in the development of electrode materials, the aim of this study was to investigate the synergistic effect of CDs synthesized from PD derivatives with varying physical and chemical properties on the electrochemical performance of SCs.

In this work, we report the preparation of multicolored fluorescence CDs with green, yellow, and red emissions using facile hydro/solvothermal and microwave-assisted solvothermal methods with three different PD isomers (m-PD, o-PD, and p-PD). The prepared CDs emit a strong and stable luminescence in solution under single-wavelength ultraviolet light excitation. The effect of these PD-derived CDs on capacitance performance was investigated by using them as electrodes in both symmetric and asymmetric SCs, without the addition of hybrid or conductive materials. To better assess their suitability for practical applications, the synthesized CDs were utilized in a two-electrode SC system, thereby providing an innovative approach to address the limitations of CDs and enhance SC performance, thereby contributing significantly to the existing literature. The performance, rate capability, and cycling stability of the SC were evaluated by considering the properties of each component in the device design. In addition, structural defects in the material structure were also studied to determine the influence of PD isomers on CD synthesis. The improved electrochemical properties of these pure CDs used in SCs may provide significant contributions to studies on enhancing the performance of CD-based composite electrodes in future SC designs.

2. Experimental Section

2.1. Materials

m-PD (Sigma Aldrich, 98%), o-PD (Merck, 98%), and p-PD (Alfa-Aesar, 98%) were used as starting precursors in the synthesis of multicolor CDs. Ethanol (Isolab 98%) was used as a solvent. The Milli-Q system purified ultrapure water throughout the experiments (Millipore Inc., $\Omega = 18 \text{ M}\Omega \text{ cm}$).

2.2. Synthesis of CDs from PD Derivatives

Green-to-red tunable fluorescence CDs were prepared from PD derivatives and carbonized under different reaction conditions.

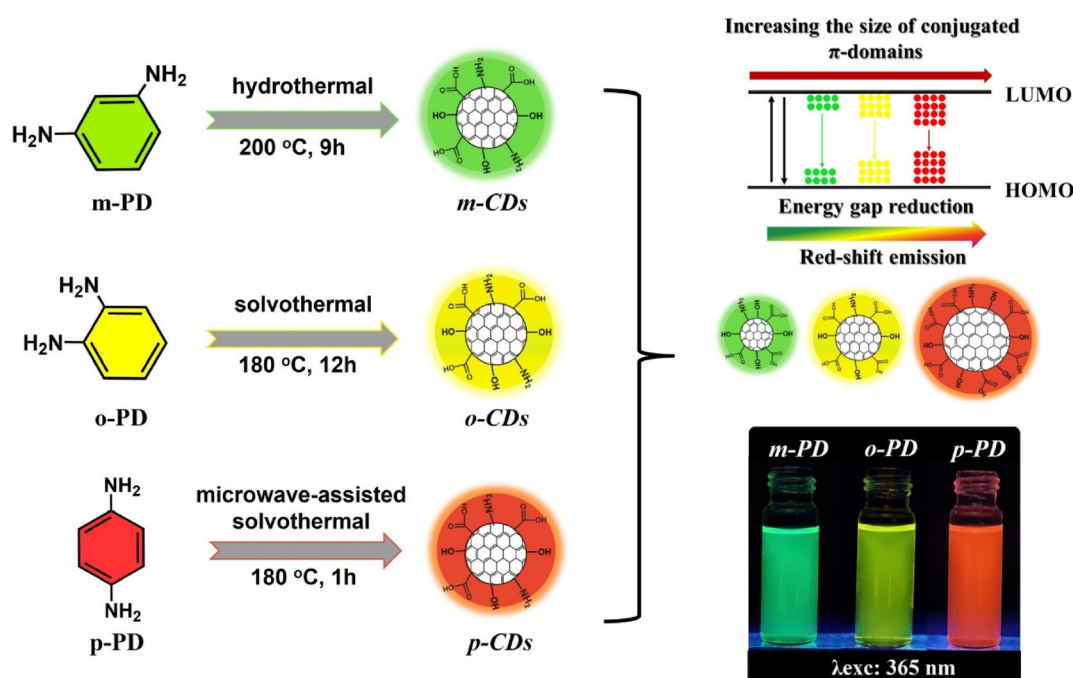


Figure 1. Schematic illustration of multicolor CD synthesis from PD derivatives.

CDs with green and yellow emissions were synthesized using the one-pot hydro/solvothermal method without the acids used as engineering reagents and the precursors (**Figure 1**).^[33,34] Green-emitting CDs: 0.020 g (0.185 mmol) of m-PD was sonicated in 10 mL of water until a homogeneous mixture was formed. It was then transferred to a 25 mL Teflon-coated stainless steel autoclave and heated at 200 °C for 9 h. Yellow-emitting CDs: 0.1 g (0.925 mmol) of o-PD was sonicated in 10 mL of ethanol until a homogeneous mixture was formed. It was then transferred to a 25 mL Teflon-lined stainless steel autoclave and heated at 180 °C for 12 h. After the resulting solutions were cooled to room temperature, they were centrifuged at 8000 rpm for 10 min. The supernatant was collected and dried in an oven at 90 °C. Red-emitting CDs: The microwave-assisted solvothermal method we reported in our previous study was used.^[35] A 0.028 g (0.258 mmol) p-PD was sonicated in 25 mL of an ethanol/water (1:1, v/v) solution until a homogeneous solution was formed. The resulting mixture was transferred to the Teflon containers of the microwave synthesis apparatus, and the reaction was carried out for 1 h at a constant temperature of 180 °C. After cooling to room temperature, the solution was centrifuged at 8000 rpm for 10 min. After centrifugation, the supernatant was dried in an oven at 90 °C. CDs were purified by silica column chromatography using a mixture of methyl alcohol and dichloromethane as the eluent. According to their starting precursors, CDs with green, yellow, and red emissions are coded as m-CDs, o-CDs, and p-CDs, respectively.

2.3. The Preparation of SC Design with a Two-Electrode Setup

Using a two-electrode system, the electrochemical characteristics of CDs made from various isomeric (*ortho*-, *meta*-, and *para*-)

structures of PD as precursors were investigated as part of the study. Our two-electrode system utilizes powdered electrode materials that can be directly employed without pretreatment. The CDs were directly used as active electrode materials without any additional binders or conductive additives, highlighting their intrinsic electrochemical properties. Depending on the design, the total mass of active material used for both electrodes ranged from 1 to 2 mg. The mass of each electrode was precisely controlled using a high-precision balance to ensure consistency across different samples. The excellent stability of CDs in aqueous solutions was confirmed by their ability to maintain a homogeneous phase for 72 h, as shown in Figure S2, Supporting Information. This stability is attributed to their robust carbon core structure and surface functionalization, which prevents dissolution in the electrolyte during charge–discharge cycles while maintaining efficient electrochemical performance. The hydrophilic surface groups (O–H and N–H) facilitate controlled interaction with the electrolyte without compromising structural integrity. In the original design of the SC, as depicted in **Figure 2**, stainless steel screws are employed as current collectors. The powder-form CDs were carefully spread over the flat contact surface of each stainless steel screw using a spatula to ensure homogeneous surface coverage. After this manual distribution, the partially assembled cell was exposed to mild sonication (≈ 30 s) to assist in the uniform packing and surface adhesion of the powder layer. Following the addition of the first electrode material (E_1) in powdered form to a screw, a glass fiber separator and the second electrode (E_2) are subsequently placed. A specific quantity of electrolyte solution was poured onto the electrode and separator using a micropipette. A ≈ 40 μ L of 6 M KOH electrolyte was applied to the separator using a micropipette to ensure complete ionic contact. The screws were then fastened, as

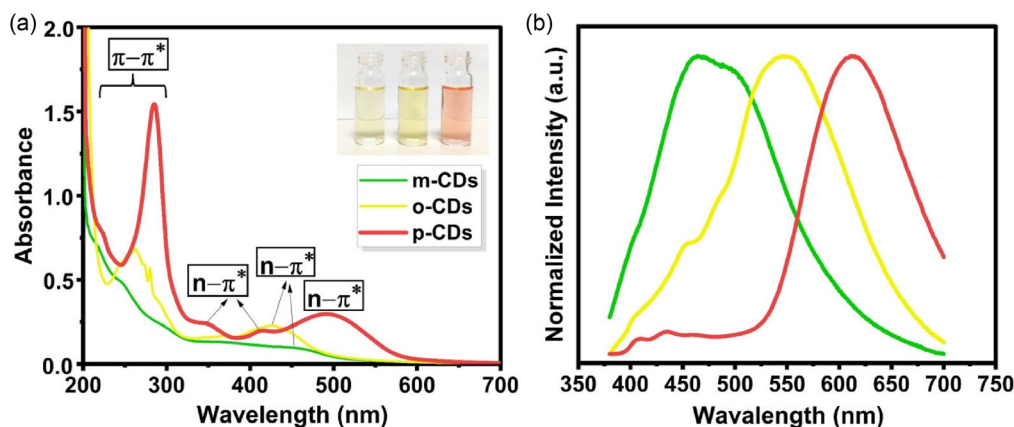


Figure 2. a) UV-vis absorption and b) normalized fluorescence emission spectra of CD samples measured in ethanol (inset: photographs of m-CD, o-CD, and p-CDs under bright light, from left to right).

depicted in Figure S1, Supporting Information, and electrochemical analysis was conducted. Additionally, the second electrode in the asymmetric configuration was composed of commercially available activated carbon (AC) from Kuraray Chemicals. Since the synergistic interaction with CDs is essential for electrochemical performance, AC, which is known to have a high surface area, was used as the second electrode. Throughout the long-term electrochemical testing, no visible delamination, powder displacement, or electrode degradation was observed, even after 10,000 continuous charge/discharge cycles. This confirms that the electrode architecture, despite the binder-free design, maintained excellent mechanical stability under practical operating conditions.

2.4. Characterizations

Ultraviolet-visible (UV-vis) absorption spectra were recorded using an Analytic Jena Specord 210 spectrometer over a wavelength range of 200–800 nm. The fluorescence emission spectra of CDs in ethanol solutions were obtained using an F55 Spectrofluorometer (Edinburgh Instruments) with excitation at 360 nm. Fluorescence images of CD solutions were captured using a UV lamp (254/365 nm, UVP UVGL-58, Analytik Jena). The morphology and particle size of the synthesized CDs were determined using Transmission electron microscope (TEM) (Model JEOL JEM-ARM20CFEG UHR-TEM). The mean particle core size (r) and standard deviation were calculated by measuring the diameter of at least 50 particles using ImageJ. The hydrodynamic radius (R_h), zeta potential (ζ -Pot), and electrical conductivity (σ) measurements were performed using a dynamic light scattering (DLS) instrument (Zetasizer Nano-ZS, Malvern Instruments). Fourier transform infrared spectroscopy (FT-IR) (Bruker Tensor 37 spectrometer) was used to determine the chemical structure and composition of CDs, covering the range from 4000 cm^{-1} to 600 cm^{-1} . The Raman scattering spectra were measured on a Raman spectrometer (Renishaw, In Via Qontor) at an excitation laser wavelength of 532 nm.

Electron paramagnetic resonance (EPR) investigations were conducted by a Bruker Benchtop EMX Nano EPR spectrometer,

equipped with an integrated referencing system for g-factor determination and a spin counting unit. The EPR spectra were acquired at room temperature using a resonator with a microwave frequency of 9.63 GHz. These measurement conditions ensured consistent and controlled EPR data acquisition, enabling the examination of the electron spin properties of the studied samples.

The developed SCs were tested using potentiostatic electrochemical impedance spectroscopy (PEIS), cyclic voltammetry (CV), and galvanostatic cycling with potential limitation (GCPL) analyses, with the manufactured CDs serving as electrode materials. The studies were conducted within the voltage range of 0–1 V, using 6 M KOH as the electrolyte. The impedance analysis of the SCs was conducted over a broad frequency range spanning from 1 MHz to 10 MHz. A wide range of scanning rates (1–200 mV s^{-1}) was employed to examine the CV, spanning from high to low scanning speeds. The GCPL test measured various current densities ranging from 0.1 A g^{-1} to 2.4 A g^{-1} . Figure 2 shows the schematic representation of the SC, and Table 1 shows its content, both of which were created for electrochemical characterization experiments.

The specific capacitance (F/g), energy density (Wh/kg), and power density (kW/kg) of all fabricated SCs were determined using the following equations. Specific capacitance (C_s) was calculated based on the CV curve analysis. In the given equation, the current (I in A) denotes the specific current; the operational voltage window is expressed by dV (V), the scan rate is represented by v (mV/s), and m (g) indicates the mass of the active electrode material. The variables are systematically outlined as follows

Table 1. Comprehensive details regarding each component of the SC design.

Sample	Electrode (E_1)	Electrode (E_2)	Electrolyte (EI)	Separator (S)	Type
o-CDs	o-CDs	o-CDs	6 M KOH	Glass fiber	Symmetric
m-CDs	m-CDs	m-CDs	6 M KOH	Glass fiber	Symmetric
p-CDs	p-CDs	p-CDs	6 M KOH	Glass fiber	Symmetric
m-CDs//AC	m-CDs	AC	6 M KOH	Glass fiber	Asymmetric

$$C_s = \frac{\int_{V_1}^{V_2} I(V) dV}{2m\Delta V} \quad (1)$$

$$\text{Energy Density, } E = \frac{0.5 * C_s * \Delta V^2}{3.6} \quad (2)$$

$$\text{Power Density, } P = \frac{E}{(\Delta t / 3600)} \quad (3)$$

In these equations, C_s denotes the specific capacitance in Farads per gram (F/g), ΔV is the total potential window in volts (V), E is the energy density, and Δt represents the discharge time in seconds. Equation (2 and 3) were employed to calculate the energy and power densities of the produced electrodes, respectively.

3. Results and Discussions

3.1. Characterization of Multicolor CDs

The synthesis of full-color emission CDs from green to red, as shown in Figure 1, was carried out by carbonization of PD derivatives in specified ratios under different reaction conditions using solvothermal and microwave-assisted solvothermal methods. The obtained CDs in ethanol solutions displayed a clear color under daylight and exhibited bright fluorescence colors, ranging from green to red, under 365 nm UV light.

Figure 2a displays the UV/vis spectra of multicolor CDs. The UV–vis absorption spectra of these three CDs showed significant optical absorption in the UV region, with a tail extending into the visible range. The peaks exhibited by CDs in the UV region (between 200 and 300 nm) correspond to the π – π^* transitions of C=C.^[16,36,37] However, CDs exhibited different absorptions in the more extended wavelength region. The three samples exhibit different absorption maxima/bands at 348, 413, 426, 456, and 492 nm, attributed to the n – π^* transition of C=O and C=N bonds, identifying the presence of aromatic structures.^[14,35] This suggests that CDs have different surface state transitions.^[36,38]

Multicolor m-CDs, o-CDs, and p-CDs synthesized using different PD derivatives exhibited maximum emission peaks with red-shifts at 451, 490, and 604 nm, respectively, when excited at 360 nm (Figure 2b). In addition, the fluorescence QYs of CDs in ethanol were calculated using quinine sulfate, rhodamine 6 G, and rhodamine B as standards (Table 2, Table S1, Supporting Information). Compared to the rhodamine 6G reference, m-CD exhibited green emission, and o-CD exhibited yellow emission, demonstrating the highest QY at 64.49% and 77.40%, respectively. p-CD exhibited 39.15% (λ_{exc} :365) and 48.08% (λ_{exc} :520)

QY compared to rhodamine B. Additionally, the aqueous solution of CDs maintained a homogeneous phase for 72 h, indicating the excellent long-term stability of the synthesized CDs (Figure S2, Supporting Information). It is known that the fluorescence behavior of CDs is based on the complex relationships between the carbon core and the surrounding chemical groups. The origin of the fluorescence color of CDs is due to the electronic bandgap transitions of conjugated π -domains and surface defect states due to surrounding chemical groups (Table 2).^[16,39] The sp^2 hybridized carbon nuclei that form the basis of CDs have a dynamism in which the bandgap varies depending on the sp^2 conjugation length or size. As the particle size increases, the bandgap decreases with increasing conjugated π area, indicating a tunable blue-to-red fluorescence emission.^[39,40] Supporting this, the electronic bandgap calculated from UV/vis and photoluminescence data increased with decreasing particle size (Table S2, Figure S3–S4, Supporting Information). The particle size of CDs has a significant impact on electron mobility. While smaller particles may exhibit reduced mobility due to the increased bandgap resulting from quantum confinement, they also offer shorter transport paths and improved surface contact, which can facilitate more efficient electron hopping and interfacial charge transfer. Smaller particles provide a more uniform distribution in the electrode matrix in SC construction. This allows electrons to follow shorter, more continuous paths from one point to another, thus increasing overall conductivity and mobility.^[41,42]

Table 2 outlines the physical characteristics of the synthesized CDs. DLS measurements reveal that all CDs had an Rh under 75 nm. TEM images in Figure 3 show a uniform distribution in size and shape, with an r of 6.09 ± 1.64 , 8.32 ± 1.17 , and 8.54 ± 4.11 nm for m-CDs, o-CDs, and p-CDs, respectively. The steric and electronic properties of the precursor molecules can indeed explain the size distribution of CDs synthesized from different PD isomers. The *meta*-position of the amino groups in m-PD minimizes steric hindrance, facilitating more efficient and compact nucleation and growth processes, which results in smaller CDs. In contrast, the *ortho*- and *para*-positions in o-PD and p-PD introduce more steric hindrance and less favorable electronic conditions, leading to larger CDs. This observation aligns with studies on the influence of precursor structure on the properties of CDs, where the positioning of functional groups in precursor molecules significantly impacts the size and characteristics of the resulting CDs. For instance, different isomers can alter the interaction dynamics and aggregation behavior during the synthesis, affecting the nucleation and growth of CDs.^[43–45] The discrepancy between Rh and r values might be due to the formation of an electrically charged double layer surrounding the particles in DLS.^[16,46,47]

Table 2. Physical properties of synthesized CDs. λ_m and QY were measured. TEM image analysis calculated the mean diameter of the CD's core. The samples' Rh , ζ -pot, and σ_c were measured in milli-Q water.

Samples	λ_m [nm]	QY [%]	Size by TEM [d.nm]	Rh [d.nm]	ζ -Pot [mV]	σ_c [S/cm]
m-CDs	480	64.49	6.09 ± 1.64	39.10 ± 6.60	2.26 ± 0.38	5.00 ± 0.20
o-CDs	548	77.40	8.32 ± 1.17	47.13 ± 8.01	1.79 ± 0.22	4.44 ± 0.07
p-CDs	614	39.15	8.54 ± 4.11	75.68 ± 11.11	1.52 ± 0.17	4.43 ± 0.03

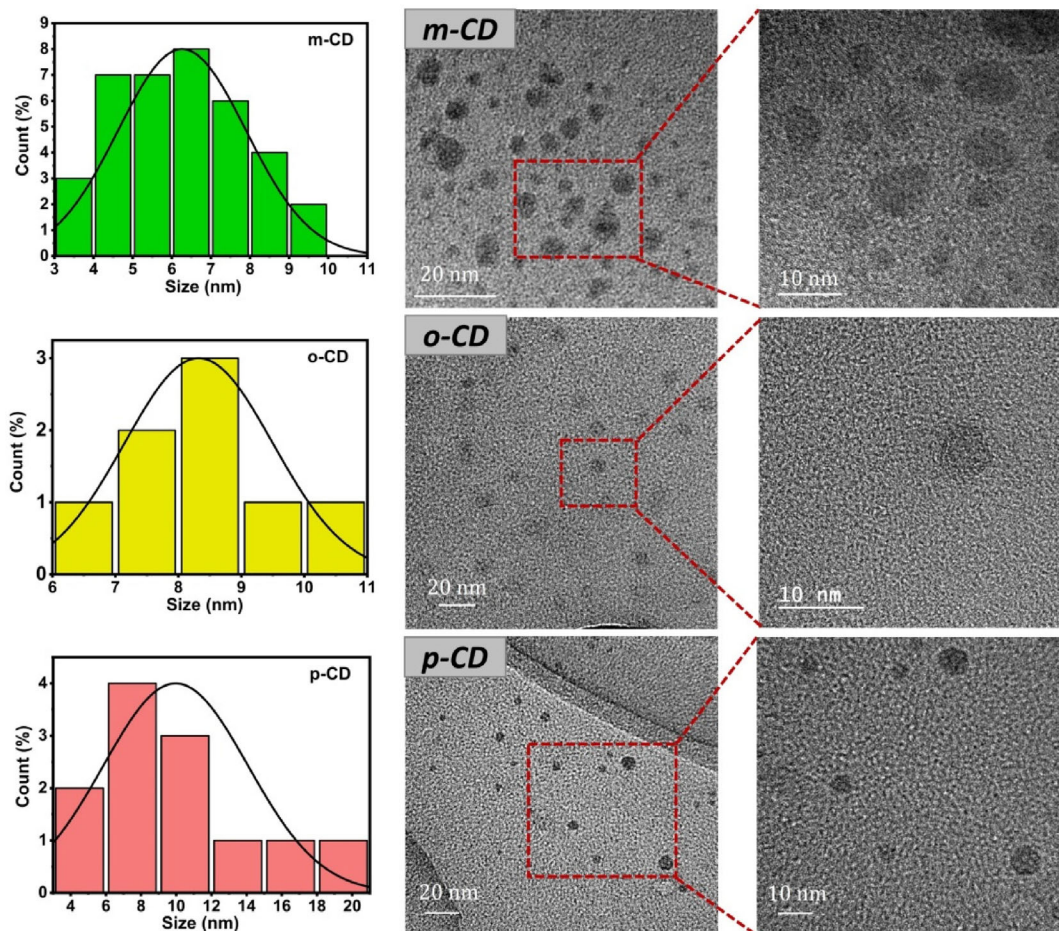


Figure 3. TEM images of carbon quantum dots and the size histogram of CDs curve-fitted to the data using the Gaussian model.

A ζ -potential measures the potential difference between a dispersed particle and its surrounding liquid, indicating surface electropositivity. This potential varies with the solution's pH during chemical reactions. In the dispersing liquid, negatively charged ions (OH^-) move toward the particle surfaces, forming the Stern layer. In contrast, H^+ ions lower the pH and shift the zeta potential in a positive direction. An increase in electropositivity from *para*- to *meta*-CDs was observed, which enhanced the attachment of oppositely charged ions to the surface, thereby increasing the material's capacity. In other words, the presence of negatively charged functional groups (carboxyl, hydroxyl groups, etc.) on the CD's surface is less than the positively charged functional groups (amine, carbonyl, epoxy, methyl (CH_3) groups, etc.), causing the particle ζ -pot to be positive.^[48,49] Table 2 indicates surface charges of 2.26 ± 0.38 , 1.79 ± 0.22 , and 1.52 ± 0.17 mV for *meta*- to *para*-CDs, respectively. A higher zeta potential signifies a greater ability of the positively charged surface to hold more charges, thus increasing the specific capacity of the material. Additionally, the conductivity of CDs in the solvent diminishes from *meta*- to *para*-CD. The *m*-CDs with green emission demonstrated the highest conductivity at 5.00 S cm^{-1} , whereas *p*-CDs with red emission showed the lowest at 4.43 S cm^{-1} . This higher conductivity in *m*-CDs is attributed to intrinsic defects on the CD surface that facilitate electron

transfer.^[19] Furthermore, the reduced particle size of CDs leads to shorter charge transport pathways, increased surface area for ion adsorption, and more efficient electron leakage networks, all of which contribute to enhanced overall conductivity.^[50]

Figure 4 presents the FT-IR and Raman spectra of CDs synthesized from different PD isomers. Figure 4a displays the FT-IR spectra, which reveal the presence of various functional groups. The hydrophilic groups, O–H and N–H, are observed between 3000 and 3500 cm^{-1} across all CDs, contributing to their solubility in polar solvents. C=O stretching vibrations are noted between 1720 and 1685 cm^{-1} and C–O stretching vibrations appear between 1100 and 1000 cm^{-1} .^[16,51] Minor peaks at 3000 to 2800 cm^{-1} correspond to the sp^3 C–H stretching vibrations.^[35,36] Importantly, there is an increase in the intensities of the C=N stretching vibrations between 1600 and 1640 cm^{-1} and C=C between 1500 and 1495 cm^{-1} , indicating a redshift in photoluminescence from *m*-CDs to *p*-CDs.^[38] This shift suggests a rise in nitrogen-containing polyaromatic structures within the CDs. Specific peaks related to the disubstituted benzene rings are detected at $750\text{--}810 \text{ cm}^{-1}$ for *m*-PD, $735\text{--}770 \text{ cm}^{-1}$ for *o*-PD, and $790\text{--}840 \text{ cm}^{-1}$ for *p*-PD.^[35,52] The C=N and O–H/N–H groups on the surface of CDs, especially when they are in a π -conjugated structure, create local regions with high electron density. These regions facilitate the adsorption of ions to the surface by

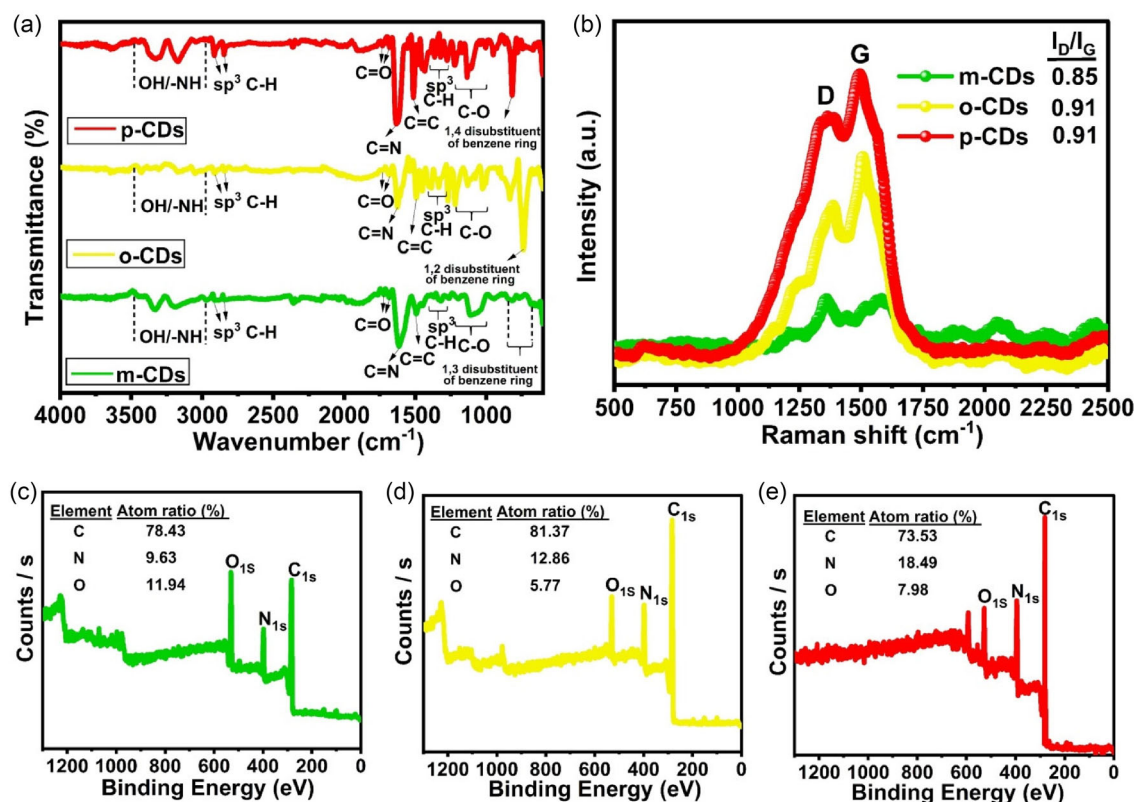


Figure 4. Spectroscopic analysis of CDs derived from different PD isomers: a) FT-IR spectra showing the presence of functional groups; b) deconvolution of Raman spectra with I_D/I_G ratios for m-CDs, o-CDs, and p-CDs; and c–e) XPS survey spectra of CDs. The atomic ratios (%) of the elements are listed in the inset table.

establishing electrostatic interactions with cationic species (e.g., K^+ ; H^+). Additionally, groups such as $C=N$, which can act as electron donors or acceptors, enhance electron mobility by creating charge transfer paths within the CDs. In this way, high conductivity is provided in redox reactions. These groups facilitate charge redistribution and promote stronger interactions with electrolyte ions, improving ion adsorption and surface charge accumulation.^[41,53]

Figure 4b shows the Raman spectra, which illustrate two distinct peaks corresponding to the D and G bands, indicating the structural properties of the carbon atoms within the CDs. The D band, related to the defects in the carbon structure, appears at about $1355\text{--}1360\text{ cm}^{-1}$, and the G band, associated with the in-plane vibrations of sp^2 carbon atoms in a hexagonal lattice, is found at $1495\text{--}1580\text{ cm}^{-1}$. The I_D/I_G ratios, reflecting the degree of structural defects, are 0.85 for m-CDs and 0.91 for both o-CDs and p-CDs, suggesting the presence of multiple defects across these variants. This ratio also confirms that the synthesized CDs are amorphous, rather than graphene quantum dots (GQDs), aligning with their unique electronic properties, which are necessary for diverse applications.^[54,55] The I_D/I_G ratio in Raman spectroscopy measures the intensity of the D band (defect-induced) to the G band (graphitic). A lower I_D/I_G ratio typically means fewer defects and a higher degree of graphitization.^[56,57] The intensity of the G band is higher than the D band, indicating that the CDs are mainly sp^2 carbons with some sp^3 hybrid carbons. Therefore, CDs consist mainly of sp^2 graphitic

carbons with sp^3 carbon defects.^[58] The m-CDs likely have a more uniform and less defective structure, as indicated by the lower I_D/I_G ratio. Therefore, it can be said that m-CDs have fewer structural defects and a higher degree of sp^2 hybridized carbon atoms.

Additionally, the surface chemistry and elemental composition of the CDs were characterized using X-Ray Photoelectron Spectroscopy (XPS). As shown in Figure 4c–e, the four peaks at $\approx 531\text{ eV}$, 400 eV , and 285 eV correspond to $O1s$, $N1s$, and $C1s$, respectively. Higher in o-CD (12.86%) and p-CD (18.49%) compared to m-CD (9.63%) indicates a nitrogen content composition.

Figure S5, Supporting Information, presents the high-resolution (HR) deconvolution XPS spectra for $C1s$, $N1s$, and $O1s$ in the series of synthesized CDs. The HR-XPS of $C1s$ spectra (Figure S5a, d, g, Supporting Information) exhibit distinct peak structures. In Figure S5g, Supporting Information, a single sharp $C1s$ peak is visible for p-CD, while a broad peak is visible for m-CD (Figure S4a, Supporting Information) and o-CD (Figure S4d, Supporting Information) samples. This peak is attributed to the presence of more $C=O$ bonds in the m-CD and o-CD samples compared to the p-CD sample. The three deconvoluted peaks from low to high correspond to the $C-C/C=C$ bond ($\approx 284.8\text{ eV}$ – 284.4 eV), indicating an sp^2 hybridized carbon network contributing to the electronic structure of CDs.^[59,60] The presence of $C=O$ functional groups in all CDs ($\approx 286.0\text{--}286.8\text{ eV}$) indicates the oxidation of the carbon skeleton, which may play a role in the photoluminescent properties.^[59,61] In addition, there is a peak at $\approx 288.0\text{ eV}$ in m-CD and o-CD samples, indicating the presence

of C=O bonds.^[61,62] In the N1s spectra (Figure S5b, e, h, Supporting Information), two deconvolution peaks are visible. The lower energy one (400.0 eV) is attributed to the so-called pyridinic C–N bond, while the higher energy one (398.6 eV–398.9 eV) is due to the C–NH₂/pyrrolic peaks.^[63,64] The O1s spectra (Figure S5c,f,i, Supporting Information) reveal two separated peaks around 529.5–534.0 eV, which are typically associated with carbonyl oxygen (C=O) and C–O–C bonds.^[65,66] The C=O bond is dominant in both the O1s and C1s spectra for the m-CD and o-CD samples.

3.2. Electrochemical Performance of Multicolor CDs

EPR is uniquely capable of detecting paramagnetic centers, such as carbon radicals and dangling bonds, which are indicative of defects within the materials. These defects can significantly influence the electronic properties, and consequently, the electrochemical performance. Understanding the nature and concentration of these defects is crucial for optimizing the material for SC applications.^[67] Here, various CD samples obtained from PD were analyzed via continuous-wave EPR at room temperature. The microwave power saturation dependencies can be obtained from EPR, which also gives detailed information on the conduction behavior of the samples.^[68] It is known that easily saturated samples have more electrons in the conduction state. Based on this fact, the EPR spectra in Figure 5a and b indicate the presence of paramagnetic carbon radicals or carbon defect centers, such as dangling bonds at the surface. The g-factor of all samples in Table 3 deviates slightly from the free electron g-factor ($g = 2.0023$) and their linewidth.^[68] The differentiation involving sp^2 - and sp^3 hybridization can be achieved by considering the EPR wavelength linewidth (ΔB). The values for sp^3 -hybridized carbon centers have been confirmed to be less than 1 mT for ΔB (sp^3). Graphitic carbon centers with sp^2 hybridization typically exhibit extended EPR line widths, with ΔB (sp^2) \geq 1 mT, as described.^[19] The current study provides the variation of ΔB in Table 3. Based on the abovementioned information, this research can experimentally differentiate the challenging problem of defect assignment from the carbon hybridization state.^[19]

	m-CDs	o-CDs	p-CDs
g-factor	2.00605	2.00637	2.00697
Linewidth (mT)	1.10	1.30	1.15
MW-power saturation (mW ^{0.5})	0.88	0.70	1.12

The results provide strong evidence for the presence of many unpaired electrons, which create carbon radicals and indicate the presence of sp^2 hybridization.^[19] The existence of dangling bonds can be excluded in this case, additionally, the peak-to-peak intensities of the EPR profiles for each sample increase as the microwave power increases.

In the analysis of EPR spectroscopy, systems that saturate easily typically exhibit longer relaxation times, whereas those that are harder to saturate have shorter ones. EPR also enables us to investigate the microwave power saturation behavior of the CDs, providing detailed information on the conduction behavior and the stability of the paramagnetic centers. This aspect of EPR is beneficial for understanding the electronic environment and the distribution of defects within the CDs. Microwave power-dependent measurements reveal that the o-CD samples exhibit more stable behavior compared to m-CD and p-CD samples, due to their ease of saturation, which suggests a higher concentration of carbon radicals and surface defects at lower microwave power saturation.^[68] This stability enables EPR testing below the saturation point without signal saturation, allowing for the reliable measurement of EPR intensity. Precisely determining this saturation limit will help us to obtain dependable results regarding the EPR intensity. It is essential to note that a higher linewidth results in stronger saturation points, which may also be associated with the transition to sp^2 hybridization from an EPR spectral perspective. The defect centers in p-CDs exhibit a distinct electronic environment for the unpaired electrons, which differs significantly from that of o-CDs and m-CDs.^[69] This observation strongly suggests that the response to microwave power can be attributed to the concentration of defects in the p-CDs samples, where electrons are more widely distributed (forming bound states at the

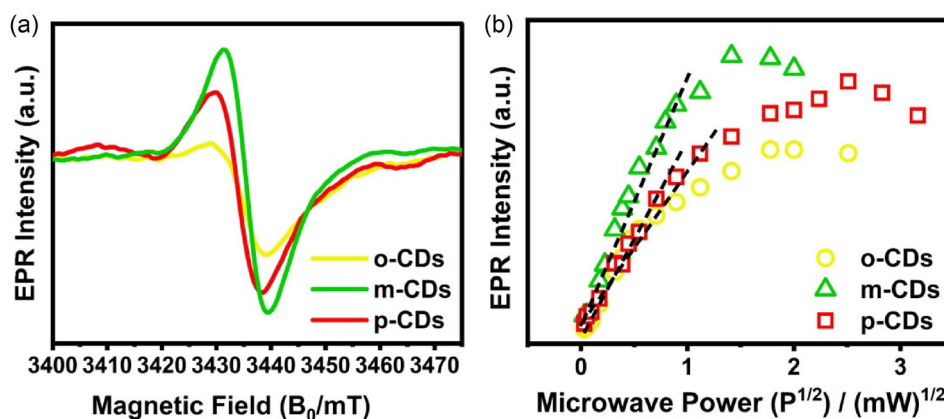


Figure 5. a) X-band EPR spectra showing the varying response of CDs derived from different PD isomers; and b) microwave radiation response behavior of CDs for highlighting differences in stability and saturation.

defect site). In contrast, the defects in the other CD samples are more confined and situated on the surface.

CV is crucial for understanding the kinetic characteristics, rates, and reaction processes of electrochemical reactions. These analyses are employed to investigate the rate and kinetics of electrochemical processes occurring on the electrode surface.^[70] The CV graphs of symmetric and asymmetric SCs, fabricated using synthesized CDs as electrodes, are displayed in Figure S6, Supporting Information, and Figure 6a. The study investigated scanning rates ranging from 1 to 200 mV s^{-1} to analyze the impact of different scanning rates. The CV curves obtained at various scan rates are presented in Figure S6, Supporting Information. The results of that study are presented in Figure S6, Supporting Information. Figure 6a displays the CV curve at a scan rate of 20 mV s^{-1} . This is performed to facilitate a more accurate comparison between SC designs and CDs synthesized using various PD isomers as precursors. Analysis of the CV curves reveals that the current in the SC varies with the isomeric structure of PD, decreasing from o-CDs to p-CDs. Moreover, a reduction in the scan rate across all samples leads to lower current values, as shown in Figure S6, Supporting Information.^[71] This decrease is due to fewer ions reaching the electrode or the electrode/electrolyte interface during slower scan rates.^[72] As the scanning rate increases, the current in the SC also rises due to enhanced ion diffusion, indicating the electrochemical stability of the materials produced. Additionally, with higher scanning rates, the anodic and cathodic current peaks shift to the right and left, respectively.^[73] This shift is indicative of the diffusion-controlled nature of the electrochemical process. In our study, CV was performed at scan rates of 10 mV s^{-1} and 1 mV s^{-1} to investigate the electrochemical behavior of the CDs. As shown in Figure S6, Supporting Information, the CV curves for m-CDs, o-CDs, p-CDs, and m-CDs//AC configurations do not display distinct redox peaks at either scan rate. This suggests that the charge storage mechanism is primarily capacitive, characterized by the quasirectangular shape of the CV curves. The absence of redox peaks indicates that electrostatic interactions, rather than faradaic processes, dominate the charge storage. This behavior is consistent with the properties of carbon-based

materials, which typically exhibit high power density and excellent cycling stability due to their capacitive nature. These findings confirm that the CDs function effectively as SC electrodes, with the m-CDs configuration showing superior performance in terms of specific capacitance and energy density. The results are detailed in the supporting file, providing a comprehensive analysis of the electrochemical behavior of our SCs.

We conducted further experiments to determine the specific capacitance values at various scan rates using electrodes made from CD-derived particles, as shown in Figure 6b. The area under each CV curve was calculated for different scan rates, and specific capacitance (F/g) was determined using calculations from the first equation.^[74] Scan rate significantly affects specific capacitance during CV measurements, influencing the kinetics of electrochemical reactions, interlayer capacitance, and the diffusion mechanism.^[75] At slower scan rates, ion transport efficiency and electrochemical processes are enhanced. This slower scanning allows for a more thorough diffusion of ions across the electrode's surface, resulting in a more uniform charge distribution. Consequently, more ions interact with the active material, increasing the specific capacitance. Reducing the scan rate can also more effectively charge the double-layer capacitance at the electrode/electrolyte interface. Thus, by managing the charging and discharging at the electrode surface, specific capacitance can be increased. A substantial increase in specific capacitance is observed as the scan rate decreases from 200 mV s^{-1} to 1 mV s^{-1} , as depicted in Figure 6b. It has been established that the capacitance of SCs is influenced by factors such as porosity, pore distribution, electrical conductivity, and particle size. As the proportion of smaller particles increases, so does the storage of electric charge. Based on the TEM and DLS results, an increase in SC capacitance is expected from m-CDs to p-CDs. Moreover, the high conductivity that m-CDs possess in facilitating electron transfer due to the inherent defects on their surface has defined m-CDs as the most effective material for SCs when used as electrodes.

Impedance analysis plays a crucial role in characterizing electrochemical systems and designing energy storage solutions. It helps to elucidate reaction mechanisms and interactions within

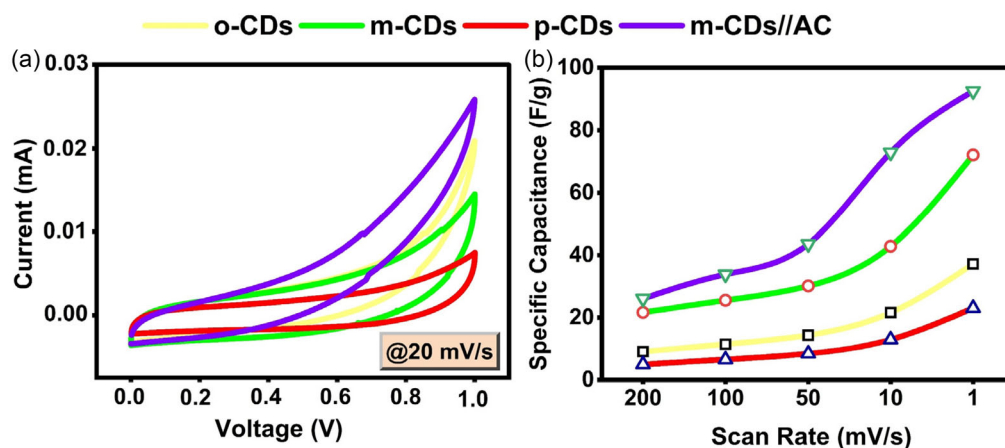


Figure 6. a) CV profiles of prepared symmetric SCs with m-CDs, o-CDs, p-CDs, and asymmetric SCs with m-CDs//AC at 20 mV s^{-1} , and b) the effect of scan rate on specific capacitance.

electrochemical systems while also determining key properties of the electrode surface, such as surface resistance and capacitance.^[76] Nyquist curves of CDs synthesized using different isomers of PD within the scope of the study are presented in Figure S7, Supporting Information, and Figure 7. The black dashed line (experimental data) in Figure S7 shows the Nyquist curve of each design. In addition, a “fitting” study was carried out on experimental data to determine the electrochemical reaction processes occurring at the electrode and electrode/electrolyte interface and the components in the equivalent circuit, and the findings are shown in Figure S7, Supporting Information, as a symbol.^[77] As shown in Figure 7, in line with the analysis, the imaginary part ($-Z_{im}$) increases in symmetrical designs as the distance between the two amino groups in the phenyl group of the PD structure rises. The increase in the $-Z_{im}$ shows that the inductive effect in the design dominates the capacitive effect. The inductance effects appear to dominate with the rise in the distance between amino groups. The real part (Z_{re}), which reflects the resistance component of the design, increases the resistance between the electrode and the electrolyte as the distance between the amino groups expands.^[78] This trend appears parallel to the imaginary component. As per Nyquist curves, the design that exhibits the lowest internal resistance is the one that utilizes m-CDs as electrodes. Compared to the symmetrical specimens, the impedance of the imaginary and real regions of the m-CDs//AC asymmetric design is lower when the Nyquist curve of the asymmetric design is checked. By employing AC with excellent conductivity and a large surface area, one can observe an augmentation in the reaction rate and the diffusion of ions at the interface between the electrode and the electrolyte. This, in turn, leads to a decrease in resistance and impedance.

Each component of the equivalent circuit derived from fitting the Nyquist curves acquired during the impedance analysis is presented in Table 4. Based on the above data, R_1 represents the resistance between the electrode surface and the electrolyte, R_2 corresponds to the charge transfer resistance of the double

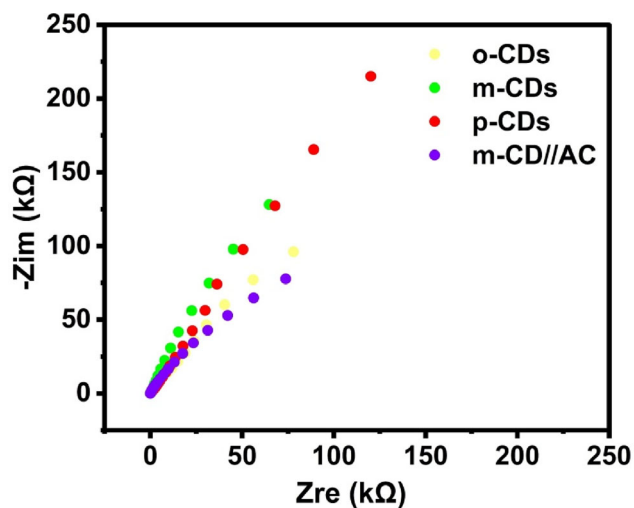


Figure 7. Nyquist curves of prepared symmetric SCs with m-CDs, o-CDs, p-CDs, and asymmetric SCs with m-CDs//AC.

Table 4. The parameters of the equivalent circuit were obtained from a fitting analysis.

Equivalent circuit $[R_1 + Q_1/(R_2 + Q_3/R_3)]^a$				
	o-CDs	m-CDs	p-CDs	m-CDs//AC
R_1	1.005	1.17	4.61	2.26
R_2	132×10^3	19.7	129×10^3	657
R_3	256×10^3	27×10^9	9.4×10^{18}	266×10^3
Q_1	33.3×10^{-6}	5.51×10^{-6}	19.8×10^{-6}	31.3×10^{-6}
Q_3	29.6×10^{-6}	37.8×10^{-6}	1.25×10^{-6}	8.84×10^{-6}
a_1	0.73	0.86	0.67	0.73
a_3	0.98	0.72	0.99	0.99

^{a)}The unit of R is ohm, and Q is $F \cdot s^{(a-1)}$. “ a ” is a constant known as the ideality factor.

layer at the electrode surface, and R_3 indicates the resistance of the material at the electrode surface. Conversely, Q_1 denotes the capacitance of the electrode surface’s double layer, whereas Q_3 denotes the capacitance of the substance on the electrode surface.^[74,79] This equivalent circuit model ($R_1 + Q_1/(R_2 + Q_3/R_3)$) was selected based on nonlinear least-squares fitting using the Z-fit module of the EC-Lab software. Among several tested configurations, this model provided the lowest chi-squared values and minimal residuals, offering the best match with experimental data across all samples. Based on this knowledge, it is evident that the resistances of R_1 and R_3 increase proportionally with the distance between amino groups. Thus, when the distance between amino groups is more significant, the resistance at the electrode/electrolyte interface and the electrode surface increases. The increase in Z_{re} and $-Z_{im}$ also indicates an understanding of this situation. Moreover, the Nyquist plot for m-CDs showed lower equivalent series resistance (R_1) and charge transfer resistance (R_2) compared to those of o-CDs and p-CDs. Specifically, the R_1 value for m-CDs was 1.17 ohms, and the R_2 value was 19.7 ohms, indicating excellent conductivity and efficient charge transfer at the electrode/electrolyte interface. This lower resistance contributes to the higher specific capacitance observed for m-CDs. The inclusion of two constant phase elements (CPEs), Q_1 and Q_3 , was crucial in capturing the frequency-dependent electrochemical response of the electrode system. The Q_1 accounts for the nonideal double-layer capacitance due to surface roughness and heterogeneity at the electrolyte interface. At the same time, Q_3 reflects distributed capacitance associated with internal porosity, chemical defects, and the intrinsic surface structure of CDs. This dual-CPE model is widely accepted for nanostructured, binder-free electrodes, where a range of time constants governs ion transport and charge storage. Conversely, when the isomeric structure changes from *ortho* to *para*, the double-layer capacitance (Q_1) and surface capacitance (Q_3) (excluding m-CDs) likewise decrease, indicating a greater ability to store charge for the SC design prepared with m-CDs. When comparing symmetric m-CDs with asymmetric m-CDs//AC in terms of design, it is observed that the R_1 and R_2 values increase with the AC contribution, while the R_3 value decreases. By utilizing carbon-based materials like AC in an

asymmetric design, a substantial increase in both double-layer resistance and double-layer capacitance (Q_1) was observed, as anticipated. Due to their exceptional conductivity and large surface area, carbon materials offer advantages in double-layer capacitance and double-layer resistance.

The accuracy of this model is further supported by the excellent overlap between the experimental and fitted impedance spectra shown in Figure S7, Supporting Information. The reduced semicircle diameter for m-CDs in Figure 7 confirms minimized interfacial resistance, while the steeper slope at low frequencies reflects more efficient ion diffusion. These features, in combination with higher Q_3 values and lower R_2 , reinforce the interpretation that m-CDs provide superior electrochemical kinetics due to their favorable surface chemistry and defect-assisted charge storage mechanisms.

The GCDPL analysis was used to characterize the charge/discharge process and cyclic performance of CDs SC designs that were synthesized using various PD isomers as precursors. This study investigated changes in the electrochemical properties of symmetrical and asymmetric SCs after 10,000 cycles. Figure 8a displays the duration of charging and discharging for all the designed SCs, specifically after the first cycle. The design that utilized m-CDs was observed to have a prolonged discharge time (Δt) compared to all other symmetrical designs. Furthermore, the utilization of m-CDs and AC in the design of an asymmetric SC resulted in comparable performance to that of m-CDs alone, with a slight increase in Δt . Particularly in designs that utilize p-CDs, Δt is significantly reduced. Furthermore, the synthesized CDs electrodes exhibit a nearly ideal capacitive behavior, as evidenced by the consistent shapes observed across all current densities in the galvanostatic charge–discharge (GCD) curves.^[80,81] Likewise, a slight decrease in electrical resistance is observed in all discharge graphs due to the ease of ion movement at the boundary between the electrolyte and electrode.

The amount of energy stored per unit weight by SCs designed within the applied voltage window range is analyzed and shown in Figure 8b. In addition, the impact of various current densities on the specific capacity was also investigated, and outcomes are illustrated in Figure S8, Supporting Information. As the current density decreases, there is a corresponding increase in the specific capacity. This phenomenon is anticipated because when the

current density is low, ions are afforded more time to infiltrate the electrode material. This enables ions to undergo efficient reactions, both at the surface and within the material's internal structure. Consequently, all the functional areas of the material can participate, resulting in an enhanced specific capacity. Moreover, the stored energy decreases when the distance between amino groups in the phenyl ring expands. Nevertheless, the SC fabricated utilizing m-CDs deviated from this trend and exhibited the highest energy storage capacity throughout the charge/discharge process. In essence, this outcome aligns with the characteristics of similar circuit components. Specifically, when examining the Q_3 value shown in Table 3, it is evident that m-CDs exhibit the highest Q_3 value, whereas the design utilizing o-CD demonstrates the lowest Q_3 value. Q_2 denotes the capacitive characteristic of electric charges accumulated on the electrode material's surface. The m-CDs design had the highest specific capacity value among the options considered. While the asymmetric design shows a slight decrease compared to the symmetric m-CDs, it exhibits enhanced energy storage capacity compared to the alternative design.

Figure 8c displays the capacitance retention values after 10 000 cycles, which were used to assess the long-term use of the fabricated SCs. The results of both the impedance analysis and the specific capacitance analysis indicate that the configuration with p-CDs exhibits a decreasing capacitance over 10 000 cycles. Furthermore, a slight decrease was observed in the design, including o-CDs. Figure 8 illustrates the stable performance of both symmetric and asymmetric designs using m-CDs, as evidenced by the absence of capacitance decrease even after 10 000 cycles. The exceptional cycling stability of the CD electrodes, particularly for m-CDs, is attributed to their robust structural integrity and controlled surface chemistry. The maintenance of capacitance over 10 000 cycles demonstrates that the CDs remain stable and do not dissolve in the electrolyte during repeated charge–discharge processes, validating their suitability as reliable electrode materials for long-term SC applications. The asymmetric configuration, utilizing m-CDs and AC, was designed to explore potential synergistic effects between these two carbon-based materials. While both materials are carbon-based, they possess distinct structural and electrochemical characteristics that can complement each other. The m-CDs, with their smaller

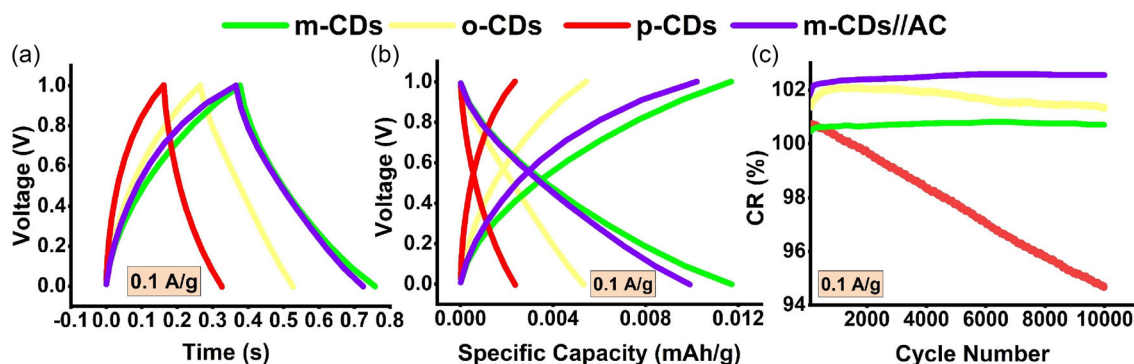


Figure 8. a) Galvanostatic charge–discharge plots; b) specific capacity; and c) capacitance retention values after 10 000 cycles of prepared symmetric SCs with o-CDs, m-CDs, p-CDs, and asymmetric SCs with m-CDs//AC.

particle size (6.09 ± 1.64 nm) and tunable surface chemistry, facilitate faster ion and electron transport, while AC provides high surface area and conductivity. This combination aims to achieve a balanced performance profile, enhancing the high power density and excellent cyclic stability of m-CDs while maintaining the high energy density of AC. The electrochemical performance of the m-CDs//AC asymmetric configuration demonstrates the effectiveness of this approach, achieving a specific capacitance of 92.5 F g^{-1} , energy density of 1.28 Wh kg^{-1} , and power density of 12.88 kW kg^{-1} . These values represent a significant improvement over the symmetric configurations, indicating successful optimization of the electrode combination. The enhanced performance can be attributed to the complementary properties of the two materials: the rapid charge–discharge capability of m-CDs and the high surface area of AC working in synergy. The integration of AC in the asymmetric design also resulted in a slight increase in the retention value of capacitance. It has been revealed that designs including m-CDs are particularly well-suited for long-term use in SCs as electrode materials. SCs were

engineered using CDs synthesized from various isomers of PDs. The corresponding electrochemical properties are detailed in Table 5. Our analysis indicates that the choice of PD isomer as a carbon precursor has a significant impact on the SC's performance. For instance, SCs using m-CDs, which have a greater distance between amino groups on the phenyl ring, demonstrated a higher specific capacitance value of 72.3 F g^{-1} . In contrast, those utilizing p-CDs, synthesized from p-PDs, showed a marked decrease in specific capacitance. This variation can be attributed to the larger particle size and higher electropositivity of p-CDs, which are factors known to influence capacitance. Additionally, Raman spectroscopy indicates that m-CDs have the lowest I_D/I_G ratio, suggesting greater structural regularity and crystallinity. Typically, a lower I_D/I_G ratio correlates with increased conductivity and specific capacitance, due to more uniform structures and fewer defects, which facilitate unrestricted electron movement and enhance electrode–electrolyte interactions. The conductivity results in Table 5 corroborate this, with m-CDs displaying the highest conductivity. Consequently, the design featuring m-CDs as electrodes, which exhibit the lowest I_D/I_G ratio, achieves the highest specific capacitance. Moreover, EPR analysis revealed that m-CDs have a higher concentration of paramagnetic centers, which correlates with their enhanced electron mobility and electropositivity.

While the specific capacitance of CDs (72.3 F g^{-1} for m-CDs) may appear lower compared to traditional AC materials, direct comparisons can be misleading due to their distinct structural and functional properties. CDs offer unique advantages that extend beyond simple charge storage capabilities. The

Table 5. The calculated electrochemical properties of the proposed SCs.

Design	Specific capacitance [F/g]	Energy density [Wh/kg]	Power density [kW/kg]
o-CDs	37.3	0.52	7.10
m-CDs	72.3	1.00	9.41
p-CDs	23.3	0.32	7.07
m-CDs//AC	92.5	1.28	12.88

Table 6. The comparison of electrochemical properties of CDs-based electrodes.

Material ^{a)}	C_s	CR [%]	P_D	E_D	Ref.
CQDs	0.66 F cm^{-2}	87.5% (4000x)	N/A	N/A	[82]
MnOx/CD/graphene	280 F g^{-1}	94.7% (10,000x)	15.63 kW kg^{-1}	19.53 Wh kg^{-1}	[83]
CQDs/PPy-NW	0.248 F cm^{-2}	85.2% (5000x)	0.224 kW h^{-1}	30.92 Wh kg^{-1}	[84]
CDs	30 F g^{-1}	N/A	N/A	N/A	[85]
α -MnO ₂ -(PPy) /CDs	$0.017 \times 10^{-3} \text{ F cm}^{-2}$	N/A	N/A	N/A	[19]
GQDs	296.7 F g^{-1}	97.6% (5000x)	0.5 kW kg^{-1}	41.2 Wh kg^{-1}	[86]
CDs/graphene	91.9 F g^{-1}	96% (10,000x)	15 mW cm^{-2}	$0.04 \times 10^{-3} \text{ Wh cm}^{-2}$	[87]
Milk-CQDs	95 F g^{-1} 40 F g^{-1}	100% (1000x)	N/A	N/A	[88]
Mn:PANI:N-CDot	595 F g^{-1}	N/A	N/A	N/A	[14]
Carbon dots/titanium dioxide	0.643 F cm^{-2}	98.4% (5000x)	$0.18 \times 10^{-3} \text{ W cm}^{-2}$	$0.024 \times 10^{-3} \text{ Wh cm}^{-2}$	[89]
KF-CQD	15.13 F g^{-1}	34.08% (200x)	N/A	N/A	[90]
Phosphoric acid functionalized carbon dots	2.08 F g^{-1}	94% (1000x)	0.075 kW/kg	0.073 Wh kg^{-1}	[91]
CQDs	144.4 F/g	77.4% (5000x)	10 kW/kg	25.8 Wh kg^{-1}	[92]
CD	19.00 F g^{-1}	98.5% (10000x)	50.00 kW kg^{-1}	2.64 Wh kg^{-1}	[16]
CD-bis16	17.64 F g^{-1}	97.5% (10000x)	$126.87 \text{ kW kg}^{-1}$	2.36 Wh kg^{-1}	
CD-bis64	32.08 F g^{-1}	98.8% (10000x)	52.12 kW kg^{-1}	4.44 Wh kg^{-1}	
o-CD	37.3 F g^{-1}	100.7% (10000x)	7.10 kW kg^{-1}	0.52 Wh kg^{-1}	
m-CD	72.3 F g^{-1}	101.3% (10000x)	9.41 kW kg^{-1}	1.00 Wh kg^{-1}	
p-CD	23.3 F g^{-1}	94.7% (10000x)	7.07 kW kg^{-1}	0.32 Wh kg^{-1}	This work
m-CD//AC	92.5 F g^{-1}	102.5% (10000x)	12.88 kW kg^{-1}	1.28 Wh kg^{-1}	

^{a)} C_s = Specific capacitance, ED and PD; energy and power density, CR; capacitance retention.

synthesized CDs demonstrate excellent cyclic stability, maintaining over 99% capacitance retention after 10 000 cycles, which is crucial for long-term energy storage applications. Additionally, m-CDs exhibit a high power density of 9.41 kW kg^{-1} , making them particularly suitable for applications requiring rapid charge–discharge cycles. The multifunctional nature of these CDs sets them apart from conventional carbon materials. Their tunable multicolor fluorescence properties, ranging from green to red emission, enable potential applications in optoelectronic devices and sensors. This dual functionality, combining energy storage capabilities with optical properties, opens up new possibilities for integrated devices where both features are desirable. Furthermore, the synthesis of CDs from PD derivatives represents a sustainable and cost-effective process that utilizes readily available precursors and environmentally friendly methods.

The superior performance of m-CDs can be attributed to their smaller particle size ($6.09 \pm 1.64 \text{ nm}$) and higher electropositivity ($2.26 \pm 0.38 \text{ mV}$), which facilitates faster electron mobility and enhanced ion transport. These characteristics, combined with their excellent conductivity ($5.00 \pm 0.20 \text{ S cm}^{-1}$), make CDs promising candidates for next-generation energy storage devices where multiple functionalities are increasingly important.

CDs are primarily utilized as electrode materials in SC systems, either in composite or functionalized forms. In this study, CDs were synthesized using various isomers of PD as carbon precursors and directly employed as electrode materials. The electrochemical performance of these CDs was then benchmarked against other CD-based electrodes reported in the literature, with the comparative results summarized in **Table 6**. PD-derived CDs exhibited exceptional electrochemical performance, particularly in terms of specific capacitance and capacitance retention, maintaining nearly their original capacity even after 10 000 cycles. Notably, the power density values also compared favorably with existing data. The use of different PD isomers as carbon precursors has proven effective for the application of CDs as both composite and pure electrode materials in energy storage systems. This study also introduces a novel electrode material with outstanding cyclic stability, expanding the current scope of electrode materials used in SCs.

4. Conclusions

In conclusion, this study evaluates the potential of CDs from m-PD, o-PD, and p-PD PD precursors as electrode materials for both symmetric and asymmetric SCs. Through a comprehensive evaluation using advanced characterization techniques, we uncovered crucial insights into the structural, optical, and chemical properties of these CDs. Among the three types, m-PD-derived CDs exhibited the most promising electrochemical performance, attributed to their smaller particle size, enhanced electropositivity, and superior ion transport properties. The results of the electrochemical tests revealed that m-CDs delivered impressive performance in both symmetric and asymmetric SCs, achieving a specific capacitance of 72.3 F g^{-1} in symmetric devices and an even higher 92.5 F g^{-1} in asymmetric configurations. This was accompanied by high energy densities of 1.00 Wh kg^{-1}

and 1.28 Wh kg^{-1} , respectively, and power densities of 9.41 kW kg^{-1} and 12.88 kW kg^{-1} . These values not only rival but, in many cases, surpass those of previously reported pure CD-based materials, positioning m-CDs as highly competitive candidates in the field of energy storage. Furthermore, m-CDs demonstrated exceptional cycling stability, retaining 101.3% of their initial capacitance after 10 000 cycles, a crucial feature for the long-term viability of energy storage devices. This study affirms the potential of CDs, particularly m-CDs, as high-performance, cost-effective, and stable materials for energy storage devices, providing a solid foundation for developing next-generation SCs with enhanced efficiency and longevity.

Acknowledgements

The authors would like to thank Mersin University Advanced Technology Education, Research and Application Center (MEITAM) for the laboratory and analysis infrastructure it provided for experimental studies.

Conflict of Interest

The authors declare no conflicts of interest.

Author Contributions

Rukan Genc and **Melis Ozge Alas Colak** planned and designed the synthesis and modification of CDs from phenylenediamine derivatives, with **Melis Ozge Alas Colak** and **Suleyman Gokhan Colak** conducting the synthesis experiments on multicolor CDs. **Rukan Genc**, **Melis Ozge Alas Colak**, and **Suleyman Gokhan Colak** also took part in data collection and analysis. **Emre Erdem** and **Ahmet Güngör**, along with **Rukan Genc**, developed the applications of CDs as electrode materials in supercapacitors and designed the EPR and PEIS studies, as well as the modeling of supercapacitor devices. Furthermore, **Emre Erdem** and **Ahmet Güngör** fabricated the supercapacitors and were responsible for data collection and analysis in these studies. The manuscript was cowritten by **Rukan Genc**, **Emre Erdem**, **Melis Ozge Alas Colak**, **Ahmet Güngör**, and **Suleyman Gokhan Colak**, who all contributed significantly to the final content. All authors have approved the final version of the manuscript and assume full responsibility for its content.

Data Availability Statement

The data that support the findings of this study are available from the corresponding author upon reasonable request.

Keywords: fluorescent carbon dots • high capacitance electrode materials • phenylenediamine isomers • supercapacitor performance

- [1] A. G. Olabi, Q. Abbas, M. A. Abdelkareem, A. H. Alami, M. Mirzaei, E. T. Sayed, *Batteries*. **2023**, 9, 19.
- [2] P. Shi, L. Li, L. Hua, Q. Qian, P. Wang, J. Zhou, G. Sun, W. Huang, *ACS Nano*. **2017**, 11, 444.
- [3] J. Yu, W. Lu, S. Pei, K. Gong, L. Wang, L. Meng, Y. Huang, J. P. Smith, K. S. Booksh, Q. Li, J. H. Byun, Y. Oh, Y. Yan, T. W. Chou, *ACS Nano*. **2016**, 10, 55204.
- [4] J. Ji, L. L. Zhang, H. Ji, Y. Li, X. Zhao, X. Bai, X. Fan, F. Zhang, R. S. Ruoff, *ACS Nano*. **2013**, 7, 6237.
- [5] S. Jayakumar, P. C. Santhosh, M. M. Mohideen, A. V. Radhamani, *J. Alloys Compd.* **2024**, 976, 173170.
- [6] O. Öztürk, E. Gür, *ChemElectroChem*. **2024**, 11, e202300575.
- [7] M. Islam, M. S. Hossain, B. Adak, M. M. Rahman, K. kubra Moni, A. S. M. Nur, H. Hong, H. Younes, S. Mukhopadhyay, *J. Energy Storage*. **2025**, 107, 114838.
- [8] B. MariaMahimai, E. Li, J. Pang, J. Zhang, J. Zhang, *J. Energy Storage* **2024**, 96, 112598.
- [9] C. Guan, J. Liu, Y. Wang, L. Mao, Z. S. Z. Fan, H. Zhang, J. Wang, *ACS Nano*. **2015**, 9, 5198.
- [10] L. Lai, H. Yang, L. Wang, B. K. Teh, J. Zhong, H. Chou, L. Chen, W. Chen, Z. Shen, R. S. Ruoff, J. Lin, *ACS Nano*. **2012**, 6, 5941.
- [11] Z. Zhai, L. Zhang, T. Du, B. Ren, Y. Xu, S. Wang, J. Miao, Z. Liu, *Mater. Des.* **2022**, 221, 111017.
- [12] M. O. Alas, F. B. Alkas, A. A. Sukuroglu, R. G. Alturk, D. Battal, *J. Mater. Sci.* **2020**, 55, 15074.
- [13] M. Semeniuk, Z. Yi, V. Poursorkhabi, J. Tjong, S. Jaffer, Z. H. Lu, M. Sain, *ACS Nano*. **2019**, 13, 6224.
- [14] M. O. Alaş, A. Güngör, R. Genç, E. Erdem, *Nanoscale*. **2019**, 11, 12804.
- [15] T. C. Wareing, P. Gentile, A. N. Phan, *ACS Nano*. **2021**, 15, 15471.
- [16] M. Ö. A. Çolak, A. Güngör, M. B. Akturk, E. Erdem, R. Genç, *Nanoscale*. **2024**, 16, 719.
- [17] M. Ö. Alaş, R. Genç, *Sustainable Material Solutions for Solar Energy Technologies*, Elsevier **2021**, 497.
- [18] C. Hu, M. Li, J. Qiu, Y. P. Sun, *Chem. Soc. Rev.* **2019**, 48, 2315–2337.
- [19] R. Genc, M. O. Alas, E. Harputlu, S. Repp, N. Kremer, M. Castellano, S. G. Colak, K. Ocakoglu, E. Erdem, *Sci. Rep.* **2017**, 7, 11222.
- [20] S. Strickland, L. Fourroux, D. Pappas, *Analyst*. **2025**, 150, 1448–1469.
- [21] Y. Y. An, X. Lin, Y. Zhou, Y. Li, Y. Zheng, C. Wu, K. Xu, X. Chai, C. Liu, *RSC Adv.* **2021**, 11, 26915–26919.
- [22] K. Jiang, S. han Sun, L. Zhang, Y. ue Lu, A. Wu, C. Cai, H. Lin, K. Jiang, C. Cai, S. Sun, D. Zhang, Y. Lu, A. Wu, P. H. rof Lin, *Angew. Chem. Int. Ed* **2015**, 54, 5360–5363.
- [23] C. Wang, Y. Fang, M. Zhang, H. Zhuo, Q. Song, H. Zhu, *Nano Res.* **2024**, 17, 4391–4399.
- [24] R. Sato, Y. Iso, T. Isobe, *Langmuir*. **2019**, 35, 15257–15266.
- [25] K. Jiang, S. Sun, L. Zhang, Y. Lu, A. Wu, C. Cai, H. Lin, *Angew. Chem. - Int. Ed* **2015**, 54, 5360–5363.
- [26] X. Lu, B. Song, L. Li, K. sik Moon, N. Hu, G. Liao, T. Shi, C. Wong, *Nano Energy*. **2015**, 17, 160–170.
- [27] Y. Y. Kannangara, U. A. Rathnayake, J. K. Song, *Chem. Eng. J.* **2019**, 361, 1235–1244.
- [28] C. Yuan, X. Liu, M. Jia, Z. L. And, J. Yao, *J. Mater. Chem. C*. **2015**, 3, 3409–3415.
- [29] J. Fang, X. Zhang, X. Miao, Y. Liu, S. Chen, Y. Chen, J. Cheng, W. Wang, Y. Zhang, *Electrochim. Acta*. **2018**, 273, 495–501.
- [30] Y. He, X. Yang, N. An, X. Wang, Y. Yang, Z. Hu, *New J. Chem.* **2019**, 43, 1688–1698.
- [31] S. G. Colak, A. Gungor, M. O. A. Colak, R. Genc, E. Erdem, *J. Energy Storage*. **2024**, 99, 113423.
- [32] A. Güngör, M. O. A. Colak, S. G. Colak, U. B. Simsek, O. C. Cosar, R. Genc, E. Erdem, *J. Energy Storage*. **2025**, 110, 115300.
- [33] D. Sengottuvelu, A. K. Shaik, S. Mishra, H. Ahmad, M. Abbaszadeh, N. I. Hammer, S. Kundu, *ACS Omega*. **2022**, 7, 27742–27754.
- [34] L. Wang, W. Li, L. Yin, Y. Liu, H. Guo, J. Lai, Y. Han, G. Li, M. Li, J. Zhang, R. Vajtai, P. M. Ajayan, M. Wu, *Sci Adv.* **2020**, 6, eabb6772.
- [35] M. Ö. Alaş, R. Genç, *ACS Appl. Nano Mater.* **2021**, 4, 7974–7987.
- [36] M. Ö. Alaş, G. Doğan, M. S. Yalcin, S. Ozdemir, R. Genç, *ACS Omega*. **2022**, 7, 29967–2998.
- [37] H. Ding, S. B. Yu, J. S. Wei, H. M. Xiong, *ACS Nano*. **2016**, 10, 484–491.
- [38] H. Ding, X. X. Zhou, Z. H. Zhang, Y. P. Zhao, J. S. Wei, H. M. Xiong, *Nano Res.* **2022**, 15, 3548–3555.
- [39] F. Yan, Z. Sun, H. Zhang, X. Sun, Y. Jiang, Z. Bai, *Microchimica Acta*. **2019**, 186, 583.
- [40] Z. Tian, X. Zhang, D. Li, D. Zhou, P. Jing, D. Shen, S. Qu, R. Zboril, A. L. Rogach, Z. Tian, X. Zhang, D. Li, D. Zhou, P. Jing, D. Z. Shen, R. Zboril, S. Qu, A. L. Rogach, *Adv. Opt. Mater.* **2017**, 5, 1700416.
- [41] J. Liu, R. Li, B. Yang, *ACS Cent Sci* **2020**, 6, 2179–2195.
- [42] H. Chen, 5, pp.1700996.
- [43] L. Ai, Y. Yang, B. Wang, J. Chang, Z. Tang, B. Yang, S. Lu, *Sci. Bull (Beijing)* **2021**, 66, 839–856.
- [44] B. Zhi, X. X. Yao, Y. Cui, G. Orr, C. L. Haynes, *Nanoscale*. **2019**, 11, 20411–20428.
- [45] S. Xue, P. Li, L. Sun, et al., *Small*. **2023**, 19, 2206180.
- [46] T. G. F. Souza, V. S. T. Ciminelli, N. D. S. Mohallem, *J. Phys. Conf. Ser.* **2016**, 733, 6–11.
- [47] A. Rahdar, N. Amini, F. Askari, M. A. Bin, H. Susan, *J. Nanoanalysis*. **2019**, 6, 80–89.
- [48] S. Setianto, L. K. Men, A. Bahtiar, C. Panatarani, I. M. Joni, *Sci. Rep.* **2024**, 14, 1996.
- [49] K. J. Mintz, M. Bartoli, M. Rovere, Y. Zhou, S. D. Hettiarachchi, S. Paudyal, J. Chen, J. B. Domena, P. Y. Liyanage, R. Sampson, D. Khadka, R. R. Pandey, S. Huang, C. C. Chusuei, A. Tagliaferro, R. M. Leblanc, *Carbon N Y.* **2021**, 173, 433–447.
- [50] Y. Wang, Q. Wang, W. Liu, X. Xin, B. Zhao, *Crystals (Basel)*. **2025**, 15, 384.
- [51] L. Li, Y. Li, Y. Ye, R. Guo, A. Wang, G. Zou, H. Hou, X. Ji, *ACS Nano*. **2021**, 15, 6872–6885.
- [52] P. Beauchamp, *Course Notes* **2010**, 2620, 19.
- [53] H. Li, Z. Kang, Y. Liu, S.-T. Lee, *J. Mater. Chem.* **2012**, 22, 24230–24253.
- [54] E. A. Stepanidenko, I. D. Skurlov, P. D. Khavlyuk, D. A. Onishchuk, A. V. Koroleva, E. V. Zhizhin, I. A. Arefina, D. A. Kurdyukov, D. A. Eurov, V. G. Golubev, A. V. Baranov, A. V. Fedorov, E. V. Ushakova, A. L. Rogach, *Nanomaterials*. **2022**, 12, 543.
- [55] V. Raveendran, A. R. S. Babu, N. K. Renuka, *RSC Adv.* **2019**, 9, 12070–12077.
- [56] T. Palaniselvam, H. B. Aiyappa, S. Kurungot, *J Mater Chem.* **2012**, 22, 23799–23805.
- [57] J. Wang, J. Tu, H. Lei, H. Zhu, *RSC Adv.* **2019**, 9, 38990–38997.
- [58] X. Ma, S. Li, V. Hessel, L. Lin, S. Meskers, F. Gallucci, *Chem. Eng. Proc. Proc. Intensif.* **2019**, 140, 29–35.
- [59] Z. Ren, J. Wang, C. Xue, M. Deng, Z. Li, H. Zhang, C. Cai, B. Xu, X. Wang, J. Li, *Chemosensors* **2023**, 11, 192.
- [60] D. Qu, Z. Sun, M. Zheng, J. Li, Y. Zhang, G. Zhang, H. Zhao, X. Liu, Z. Xie, *Adv Opt Mater.* **2015**, 3, 360–367.
- [61] T. Watcharamongkol, P. Khaopueak, C. Seesuea, K. Wechakorn, *Carbon Resources Conv.* **2024**, 7, 100206.
- [62] X. Wang, P. Yan, P. Kerns, S. Suib, L. M. Loew, J. Zhao, *J Electrochem Soc.* **2020**, 167, 147515.
- [63] M. Naushad, T. Ahamad, M. Ubaidullah, J. Ahmed, A. A. Ghafar, K. M. Al-Sheetan, P. Arunachalam, *J King Saud Univ Sci.* **2021**, 33, 101252.
- [64] Y. Yang, H. Ding, Z. Li, A. C. Tedesco, H. Bi, *Molecules*. **2022**, 27, 8627.
- [65] S. Wang, W. Sun, D. S. Yang, F. Yang, *Beilstein J. Nanotechnol* **2020**, 11, 606–619.
- [66] X. Guo, Y. Zhu, L. Zhou, L. Zhang, Y. You, H. Zhang, J. Hao, *RSC Adv.* **2018**, 8, 38091–38099.
- [67] C. V. Pham, M. Krueger, M. Eck, S. Weber, E. Erdem, *Appl Phys Lett.* **2014**, 104, 132102.
- [68] E. Erdem, *J Alloys Compd.* **2014**, 605, 34–44.
- [69] H. Kaftelen, K. Ocakoglu, R. Thomann, S. Tu, S. Weber, E. Erdem, *Phys Rev B Condens Matter Mater Phys.* **2012**, 86, 014113.
- [70] X. Pu, D. Zhao, C. Fu, Z. Chen, S. Cao, C. Wang, Y. Cao, *Angew. Chem - Int. Ed* **2021**, 60, 21310–21318.
- [71] W. Gu, M. Sevilla, A. Magasinski, A. B. Fuertes, G. Yushin, *Energy Environ. Sci.* **2013**, 6, 2465–2476.
- [72] X. Yu, A. Manthiram, *Energy Environ Sci.* **2018**, 11, 527–543.
- [73] S. Yin, Y. Wang, L. Zhao, Y. Sheng, X. Zhang, X. Huang, G. Wen, *J Colloid Interface Sci.* **2023**, 650, 1164–1173.
- [74] A. Güngör, G. Akgül, F. Bakan-Misirlioglu, E. Erdem, *Phys Scr.* **2024**, 99, 1–13.
- [75] D. O. Wipf, E. W. Kristensen, M. R. Deakin, R. M. Wightman, *Anal. Chem.* **1988**, 60, 306–310.
- [76] V. Vivier, M. E. Orazem, *Chem Rev.* **2022**, 122, 11131–11168.
- [77] A. S. Bandarenka, *Analyst*. **2013**, 138, 5540–5554.

- [78] M. E. Orazem, N. Pébère, B. Tribollet, *J Electrochem Soc.* **2006**, *153*, B129.
- [79] A. Güngör, F. Bakan-Misirlioglu, R. G. Alturk, E. Erdem, *J Energy Storage.* **2024**, *76*, 110143.
- [80] Z. Tian, X. Tong, G. Sheng, Y. Shao, L. Yu, V. Tung, J. Sun, R. B. Kaner, Z. Liu, *Nat. Commun.* **2019**, *10*, 4913.
- [81] M. Gödickemeier, K. Sasaki, L. J. Gauckler, I. Riess, *J Electrochem Soc.* **1997**, *144*, 1635–1646.
- [82] G. Chen, S. Wu, L. Hui, Y. Zhao, J. Ye, Z. Tan, W. Zeng, Z. Tao, L. Yang, Y. Zhu, *Sci Rep.* **2016**, *6*, 19028.
- [83] B. Unnikrishnan, C. W. Wu, I. W. P. Chen, H. T. Chang, C. H. Lin, C. C. Huang, *ACS Sustain Chem Eng.* **2016**, *4*, 3008–3016.
- [84] X. Jian, J. gang Li, H. min Yang, L. le Cao, E. hui Zhang, Z. hai Liang, *Carbon N Y.* **2017**, *114*, 533–543.
- [85] P. Dharmalingam, V. Ramanan, G. G. Karthikeyan, N. S. Palani, R. Ilangoan, P. Ramamurthy, *J. Mater. Sci.: Mater. Electron.* **2017**, *28*, 18489–18496.
- [86] S. Zhang, L. Sui, H. Dong, W. He, L. Dong, L. Yu, *ACS Appl Mater Interfaces.* **2018**, *10*, 12983–12991.
- [87] Q. Li, H. Cheng, X. Wu, C. F. Wang, G. Wu, S. Chen, *J Mater Chem A Mater.* **2018**, *6*, 14112–14119.
- [88] M. Athika, A. Prasath, E. Duraisamy, V. S. Devi, A. S. Sharma, P. Elumalai, *Mater Lett.* **2019**, *241*, 156–159.
- [89] W. Pholaupphon, R. N. Bulakhe, J. Manyam, I. In, P. Paoprasert, *J. Electroanal. Chem.* **2022**, *910*, 116177.
- [90] C. Baslak, S. Demirel, A. Kocyigit, H. Alatli, M. Yildirim, *Mater Sci Semicond Process.* **2022**, *147*, 106738.
- [91] V. Rimal, B. K. Singh, S. S. Mahapatra, *Full. Nanotubes and Carbon Nanostruct.* **2023**, *31*, 1096–1103.
- [92] A. Inayat, K. Albalawi, A. ur Rehman, A. Y. S. Adnan, E. A. M. Saleh, M. A. Alamri, A. A. El-Zahhar, A. Haider, S. M. Abbas, *Mater Today Commun.* **2023**, *34*, 105479.

Manuscript received: May 13, 2025
Revised manuscript received: July 1, 2025
Version of record online: July 21, 2025